

Mass spectrometry imaging of SOD1 protein-metal complexes in SOD1G93A transgenic mice implicates demetalation with pathology

Received: 24 February 2023

Accepted: 12 July 2024

Published online: 08 August 2024

 Check for updates

Oliver J. Hale¹, Tyler R. Wells², Richard J. Mead^{2,3}✉ & Helen J. Cooper¹✉

Amyotrophic lateral sclerosis (ALS) is characterized by degeneration of motor neurons in the central nervous system (CNS). Mutations in the metalloenzyme SOD1 are associated with inherited forms of ALS and cause a toxic gain of function thought to be mediated by dimer destabilization and misfolding. SOD1 binds two Cu and two Zn ions in its homodimeric form. We have applied native ambient mass spectrometry imaging to visualize the spatial distributions of intact metal-bound SOD1^{G93A} complexes in SOD1^{G93A} transgenic mouse spinal cord and brain sections and evaluated them against disease pathology. The molecular specificity of our approach reveals that metal-deficient SOD1^{G93A} species are abundant in CNS structures correlating with ALS pathology whereas fully metalated SOD1^{G93A} species are homogeneously distributed. Monomer abundance did not correlate with pathology. We also show that the dimer-destabilizing post-translational modification, glutathionylation, has limited influence on the spatial distribution of SOD1 dimers.

Mutations in the gene coding the metalloenzyme superoxide dismutase 1 (SOD1) are responsible for ~20% of familial amyotrophic lateral sclerosis (fALS) cases, an inherited disease characterized by degeneration of neurons in motor-associated regions of the central nervous system (CNS)¹. Under physiological conditions, the human wild-type SOD1 (hSOD1^{wt}) matures to form a non-covalently bound homodimer incorporating one zinc ion, one copper ion and one intramolecular disulfide bond per subunit. The canonical view is that mutations in *SOD1* destabilize the native structure of the protein, resulting in monomerization and aggregation of the protein. This pathway results in a toxic gain of function that causes degeneration of motor neurons^{1,2}. Demetalation^{3–7}, absence of the intramolecular disulfide bond⁸, loss of secondary structure⁹, monomerization¹⁰, oligomerization^{7,9,11}, and oxidative post-translational modification^{12,13} have all been associated with SOD1 misfolding. Some studies have also suggested that misfolding of

wild-type SOD1 extends to cases of sporadic ALS^{14–17}, although this remains controversial^{18,19}.

Here, we investigated the distribution of SOD1 complexes in sections of spinal cord and brain from the well-established transgenic hSOD1^{G93A} mouse model of ALS²⁰ and the transgenic hSOD1^{wt} control using a recently developed native ambient mass spectrometry imaging (MSI) methodology. Native ambient MSI is a label-free molecular imaging technique with the unique capability to identify and map the distribution of endogenous protein complexes within tissue sections, including metal-bound proteins and membrane proteins^{21–24}. Unlike mass spectrometry-based elemental imaging techniques, which provide information on total metal ion distribution within tissue but lack specificity for protein–metal binding^{25,26}, and matrix-assisted laser desorption/ionization (MALDI) MSI, in which protein distributions can be visualized but any information on metal binding is lost due to the denaturing sample preparation conditions²⁷, native ambient MSI

¹School of Biosciences, University of Birmingham, Birmingham, UK. ²Sheffield Institute for Translational Neuroscience, University of Sheffield, Sheffield, UK.

³Neuroscience Institute, University of Sheffield, Western Bank, Sheffield, UK. ✉e-mail: r.j.mead@sheffield.ac.uk; h.j.cooper@bham.ac.uk

involves direct analysis of the intact protein–metal complex. Native ambient MSI can distinguish signals specific to different numbers of non-covalently bound metal ions and post-translationally modified forms of proteins (proteoforms). Fresh-frozen tissue is analyzed intact, i.e., there is no requirement for homogenization, nor is there a requirement for the development of specific antibodies or tags. The workflow is described in Fig. 1, with amino acid sequences for wild-type mouse SOD1 (mSOD1^{wt}), wild-type human SOD1 (hSOD1^{wt}), and human G93A SOD1 (hSOD1^{G93A}) variant given in Supplementary Fig. S1 and details of the samples given in Supplementary Table S1, Supplementary Information. Our observations indicate that localized abundance of metal-deficient states of hSOD1^{G93A} is a key factor in the degeneration of motor neurons in the spinal cord and brain.

Results

Identification and characterization of protein complexes

Characterization of proteins and protein complexes detected in the CNS tissues was performed by top-down mass spectrometry after sampling with nanospray-desorption electrospray ionization (nano-DESI²⁸) under native conditions²¹, or liquid extraction surface analysis (LESA²⁹) under denaturing conditions³⁰. For brevity, details of characterization experiments are included in Supplementary Note 1, Supplementary Figs. S2–S14, and Supplementary Tables S2–S6. In summary, hSOD1^{G93A} and hSOD1^{wt} were detected as dimers binding 2, 3 (metal-deficient) and 4 (holo) metal ions, and as monomers binding 1 (metal-deficient) or 2 (holo) metal ions.

MS imaging of protein–metal complexes

Spinal cord. Motor neuron degeneration in the lumbar region of the spinal cord is well-established in the hSOD1^{G93A} mouse model^{20,31}. Representative spatial analyses of protein complexes by native ambient MSI in lumbar cord sections for each genotype (hSOD1^{wt} and hSOD1^{G93A}) are shown in Fig. 2. Ion images of each protein charge state contributing to the images in Fig. 2, and biological replicates, are included in Supplementary Figs. S15 (hSOD1^{G93A}), S16 (hSOD1^{wt}), and

S17 (monomers), Supplementary Information. We used the protein complex [Arf1 + GDP] (identified in the previous work²⁴), a molecular marker for the grey matter, to define the section outline (Fig. 2b–i) and assist with image interpretation.

SOD1 complexes were detected in multiple metal-bound states; hSOD1^{wt} was predominantly detected in the holo-form, binding a total of 4 metal ions in the dimeric complex (Fig. 2e, 2 metal ions for the monomer; Fig. 2g). Conversely, hSOD1^{G93A} was detected in metal-deficient forms, binding only 2 (Fig. 2j) or 3 metal ions (Fig. 2k) in each dimer (1 metal ion for the monomeric form, Fig. 2m), in addition to the holo-form. Metal-deficient dimers and monomers of hSOD1^{G93A} featured the same spatial distributions. We found that metal-deficient dimeric and metal-deficient monomeric hSOD1^{G93A} complexes were significantly more abundant in the ventral horn (Fig. 2o, dimers; $P < 0.01$, monomers; $P < 0.001$) than in the dorsal horn, correlating with FALS pathology. Fully metalated (i.e., dimers with 4 metal ions, monomers with 2 metal ions) hSOD1^{G93A} complexes were ubiquitous with no significant difference in abundance between ventral and dorsal horns, and high-resolution native ambient MS imaging showed lower abundance in grey matter versus white matter. This observation supports the hypothesis that the metal-deficient state is key to the disease pathology, rather than monomerization, since fully metalated monomers were also abundant in hSOD1^{G93A} dorsal horn (Fig. 2n, o). Metal-deficient complexes were not detected above baseline chemical signal in the hSOD1^{wt} spinal cord tissue. No significant difference in abundance was observed between hSOD1^{wt} complexes detected in the ventral horn and dorsal horn. Overall, signal intensity was greater for hSOD1^{G93A} than for hSOD1^{wt}, reflective of the higher expression level of SOD1 in the hSOD1^{G93A} model but not linked with disease pathology²⁰.

Examination of formalin-fixed paraffin-embedded (FFPE) tissue sections from hSOD1^{G93A} and mSOD1^{wt} littermates (Supplementary Fig. S18, Supplementary Information) confirmed the reduced numbers of motor neurons in the ventral horn at 120 days of age in the hSOD1^{G93A} model (Fig. 2p), correlating with the elevated abundance of metal-deficient hSOD1^{G93A} complexes observed in the mass

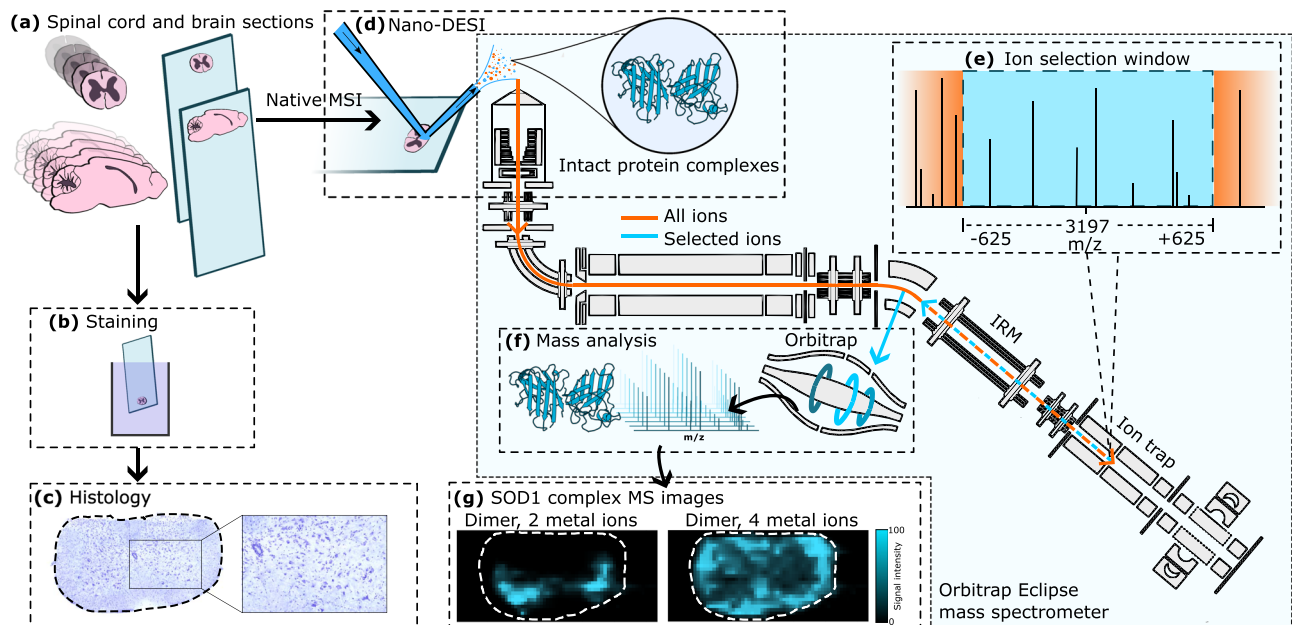


Fig. 1 | The workflow for the analysis of the spatial distribution of hSOD1^{G93A} complexes in mouse CNS tissues by native ambient MSI. **a** Serial spinal cord sections were taken in the coronal plane and brain sections in the sagittal plane. **b** Nissl staining for visualization of neurons (some sections were stained post-native ambient MSI). **c** Histology to determine motor neuron abundance. **d** Nano-DESI sampling and ionization of protein complexes directly from a tissue section.

e Protein ions were transmitted into an Orbitrap Eclipse mass spectrometer and transferred to the linear ion trap where a wide m/z selection window was applied, e.g., m/z 3197 \pm 625. The orange line represents the ion beam before m/z selection in the ion trap. The cyan line represents ions selected by the ion trap. **f** The selected ions were transmitted to the orbitrap mass analyzer for m/z measurement. **g** Protein images were generated and compared with histological data.

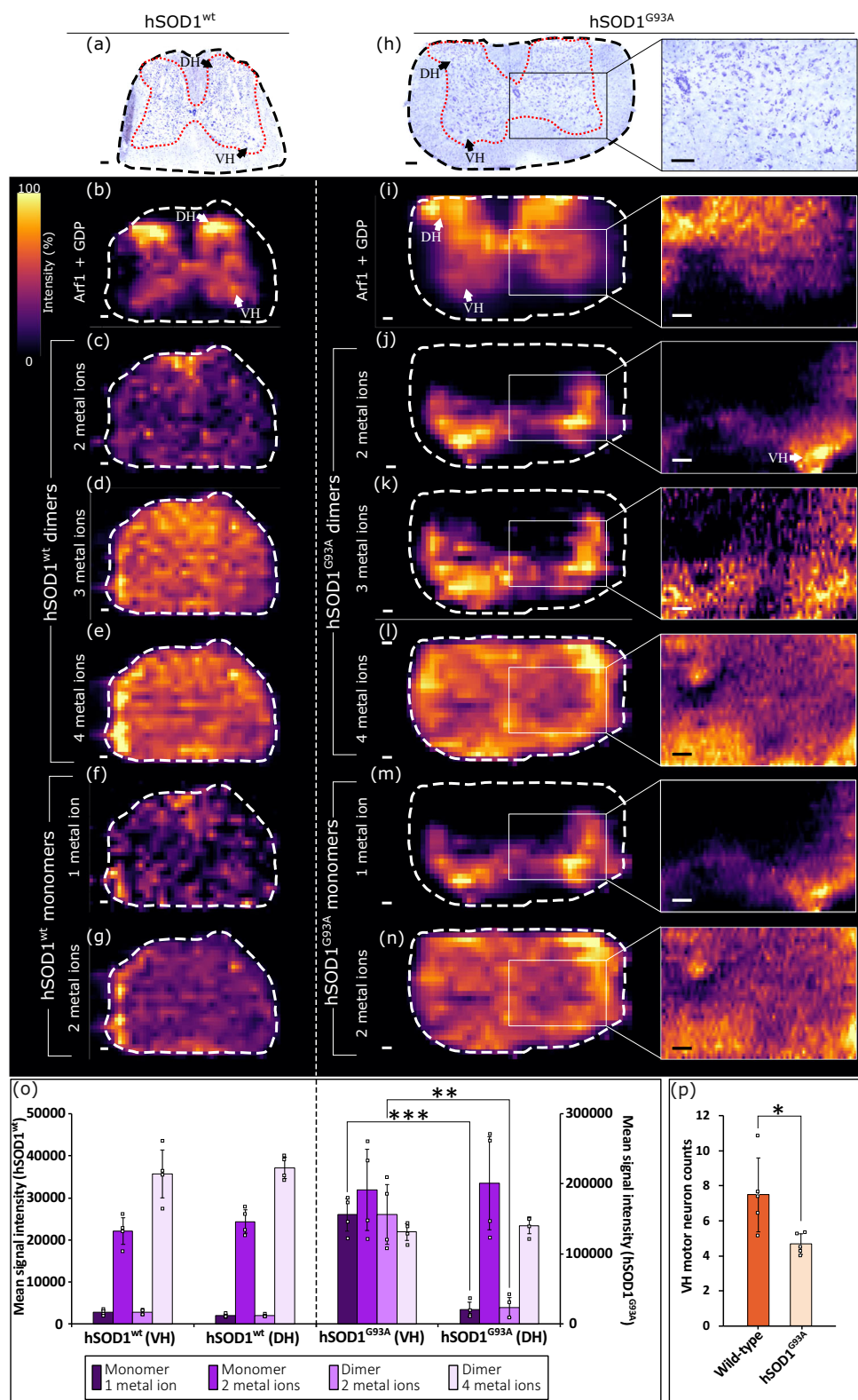


Fig. 2 | Histology and MS images of transgenic mouse lumbar spinal cord. **hSOD1^{wt}.** **a** Fresh-frozen, Nissl-stained serial tissue section (grey column indicated by the red dashed line) of spinal cord hWT-SCI (representative of 4 total sections). **b** The ion image for the Arf1+GDP complex depicts the grey matter column. Ion images for hSOD1^{wt} dimers with **(c)** two metal ions; **d** three metal ions, **e** four metal ions, and monomers with **(f)** one metal ion; **g** two metal ions. **hSOD1^{G93A}.** **h** Fresh-frozen, Nissl-stained serial tissue section (grey column indicated by the red dashed line) and expanded view of a ventral horn of spinal cord G93A-SCI (representative of 6 total sections). Ion images for **(i)** [Arf1+GDP] complex; hSOD1^{G93A} dimers with **(j)** two metal ions; **k** three metal ions; **l** four metal ions, and monomers with **(m)** one

metal ion; **n** two metal ions. White boxes show high-resolution MSI for the area indicated. **o** Evaluation of relative abundances of SOD1 complexes in DH and VH for each genotype. Data expressed as mean signal from 4 VH and DH +/- SD. **p** Average motor neuron counts (+/- SD) in mSOD1^{wt} (N = 5) and hSOD1^{G93A} (N = 5) mice in the VH of lumbar cord sections (mSOD1^{wt} N = 28, hSOD1^{G93A} N = 36) with at least 50 μ m between sections. Students' two-sided T test; * $P < 0.05$ (actual $P = 0.021$), ** $P < 0.01$ (actual $P = 2.19 \times 10^{-3}$), *** $P < 0.001$ (actual $P = 9.07 \times 10^{-5}$). DH dorsal horn, VH ventral horn. Scale bars; 100 μ m (**a–n**). MS images have one order of linear interpolation applied and a linear intensity scale. Source data are provided as a Source Data file.

spectrometry imaging experiments. Significantly lower motor neuron counts were recorded in the hSOD1^{G93A} spinal cord tissue ($P < 0.05$) with respect to mSOD1^{wt}. (Note, the mSOD1^{wt} tissue serves as a proxy for hSOD1^{wt} tissue, which was only available fresh-frozen and was unsuitable for neuron counting. Mice of both wild-type genotype do not exhibit motor neuron degeneration²⁰). We conclude that there is a critical relationship between hSOD1^{G93A} metal deficiency and the degeneration of motor neurons in the spinal cord.

Brain. Histology and native ambient MS images were obtained from hSOD1^{wt} and hSOD1^{G93A} sagittal brain sections. Figure 3 shows images for a representative analysis of each genotype. Ion images for individual protein charge states are shown in Supplementary Figs. S19, 20 (hSOD1^{wt}) and S21, 22 (hSOD1^{G93A}), Supplementary Information. Composite images for biological replicates are shown in Supplementary Figs. S23 and S24. The zinc-bound carbonic anhydrase 2 complex [CAH2 + Zn²⁺] was used as a biomolecular marker for white matter, e.g., corpus callosum (Fig. 3b–i)²⁴.

In wild-type mice, the majority of hSOD1^{wt} was detected in the holo-form, i.e., fully metalated. Lower abundance metal-deficient (2 and 3 metal ions) hSOD1^{wt} dimers were also detected localized to the hippocampal formation (Fig. 3c, d), possibly within pyramidal cells³². Holo-hSOD1^{wt} (Fig. 3e) and holo-hSOD1^{G93A} (Fig. 3l) dimers were abundant and ubiquitous throughout the sections. Holo-SOD1 is highly abundant in cerebrospinal fluid (CSF)³³, which correlates with greater signal intensity in ventricular regions and the cerebral aqueduct. Metal-deficient hSOD1^{G93A} dimers showed a notably different spatial distribution to the wild-type, with the greatest signal intensity in cranial nuclei of the brainstem and no notable abundance in the hippocampus (Fig. 3j, k). Structures related to facial motor functions, such as swallowing (e.g., hypoglossal nucleus, XII) and mastication (e.g., trigeminal nucleus, TN; facial nucleus, VII), contain degenerating motor neurons in ALS³⁴. Metal-deficient hSOD1^{G93A} was of low intensity in ventricles suggesting low relative abundance in CSF and that metal-deficient hSOD1^{G93A} complexes are formed in situ owing to the local cellular environment.

Monomeric hSOD1 was detected in both hSOD1^{wt} and hSOD1^{G93A} brains. As mentioned above, monomerization is believed to be a key event in toxic gain of function, i.e., misfolded SOD1 results in the formation of monomers that subsequently aggregate into insoluble inclusion bodies. Ion images for monomeric hSOD1^{wt} (Fig. 3f, g) and hSOD1^{G93A} (Fig. 3m, n) showed similar spatial distributions to the dimers of equivalent metal-binding state, that is, the distribution of holo-monomers (2 metal ions) matched that of holo-dimers (4 metal ions), and metal-deficient monomers (1 metal ion) matched that of metal-deficient dimers (2 or 3 metal ions). (For monomers in biological replicates, see Supplementary Fig. S25, Supplementary Information).

The region of the brainstem featuring the hypoglossal nucleus (XII) has high signal intensity for hSOD1^{G93A} dimers binding 2 metal ions. The intensity differs significantly ($P < 0.05$) to the signal intensity for the same complex in the frontal cortex (Fig. 3o), a region not associated with ALS pathology, and correlates with significantly ($P < 0.01$) lower numbers of motor neurons observed in Nissl-stained XII compared to wild-type mouse (Fig. 3p and Supplementary Fig. S26, Supplementary Information). In both regions in the wild-type genotype and in the hSOD1^{G93A} cortex, fully metalated complexes are most abundant and feature similar relative abundances. These results suggest that metal-binding state, rather than monomerization, is the key driver of pathological change. That is, the results in Fig. 3 imply a link between the localization of metal-deficient hSOD1^{G93A} and degenerating motor nuclei in the brainstem, and correlate with the results from the spinal cord.

Evaluation of metal binding and PTMs

In all cases, hSOD1 (wild-type and hSOD1^{G93A}; monomeric, dimeric, fully metalated, metal-deficient) was detected without the initiator

methionine and was acetylated at the N-terminus. Further modification by larger covalent PTMs is known to destabilize SOD1 structure and decrease its activity^{12,13,35}. Glutathionylation of hSOD1 (an additional ~305 Da per glutathionyl group) at Cys-III has been proposed to contribute to ALS pathogenesis by destabilization of the dimer interface and increasing of the dimer dissociation constant^{12,13}. We identified N-acetyl, S-glutathionyl (GS-) hSOD1^{G93A} in tissue by intact mass measurement and top-down MS. Dimers containing 1 (1GS-dimer) and 2 (2GS-dimer) S-glutathionylated hSOD1^{G93A} subunits were imaged at moderate resolution for full brain sections (composite images: Supplementary Figs. S24 and S27. Individual protein charge states: Supplementary Fig. S28, Supplementary Information). Higher resolution native ambient MSI of the brainstem revealed that metal-deficient hSOD1^{G93A} homodimers and metal-deficient 1GS-dimers (hSOD1^{G93A}/GS- hSOD1^{G93A}), each bound to 2 metal ions, exhibited the same localization, i.e., to cranial nuclei (Fig. 4a, b and Supplementary Fig. S22 Supplementary Information). The equivalent holo-dimers (i.e., 4 metal ions) were ubiquitous, with the greatest abundance in the fourth ventricle (Fig. 4c, d).

High-resolution native ambient MSI also enabled analysis of tissue structures of the cerebellum (Fig. 4e–j and Supplementary Fig. S29, Supplementary Information). The involvement of the cerebellum in ALS progression is not commonly the focus of ALS pathology, despite evidence of its importance^{36–38}. Metal-deficient hSOD1^{G93A} homodimers and hSOD1^{G93A}/GS-hSOD1^{G93A} 1GS-dimers were observed in cerebellar grey matter corresponding to the deep cerebellar nuclei (DCN)³⁹ and cerebellar peduncles (CBP) (Fig. 4g, h). Holo-homodimers were ubiquitous (Fig. 4i), but holo-1GS-dimers were most abundant in the molecular layer of the cerebellar cortex (Fig. 4j). This observation suggests an instance where spatial distribution of hSOD1^{G93A} dimers is influenced by covalent PTMs, but further investigation is required. While PTMs may play a role in SOD1 dimer destabilization and ALS progression, MSI indicates that the number of bound metal ions is the key differentiator in hSOD1^{G93A} complex localization in vivo.

Implications of hSOD1 metal-binding state

Wild-type-like SOD1 mutants such as hSOD1^{G93A} possess a mutation outside of metal-binding regions of the protein structure and enzymatic function is retained at wild-type levels^{3,20}. Demetalation is known to occur for hSOD1^{G93A}, and Cu-mediated therapeutics have been shown to improve the longevity of transgenic mice^{40–42}. Tokuda et al. developed an antibody (anti-apoSOD) specific for Cu-deficient hSOD1⁴. Extracts of homogenized tissue from the brainstem, cerebellum, and spinal cords of hSOD1^{G93A} mice were analyzed by sandwich ELISA, and signals were observed in the spinal cord extracts at the pre-symptomatic stage but not at end stage. ELISA signals were not observed for the brainstem or cerebellum samples. This result contrasts with our findings which clearly show metal-deficient hSOD1^{G93A} in regions of the spinal cord, the brainstem, and cerebellum. This discrepancy is likely because, in the ELISA experiments, the entire brainstem (~40 mg) was homogenized: Any spatial information was lost and any differential signal was averaged in the homogenate. Moreover, immunostaining of sections of the spinal cord from wild-type and hSOD1^{G93A} mice at various ages with anti-apoSOD was not successful, with significant background staining and high irreproducibility⁴. Our results demonstrate successful imaging of metal-deficient hSOD1^{G93A} in tissue sections.

The MS images presented here indicate that the accumulation of metal-deficient hSOD1^{G93A} complexes in motor-associated CNS regions is related to motor neuron degeneration. The minimum number of metal ions incorporated into hSOD1^{G93A} dimers observed in our study was two. Presumably, Zn-binding sites were occupied as studies have shown Zn incorporation to be structurally critical, enabling interaction with the copper chaperone, CCS^{43,44}. CCS is required for the maturation of SOD1 from a disulfide-reduced, copper-free state to one with an

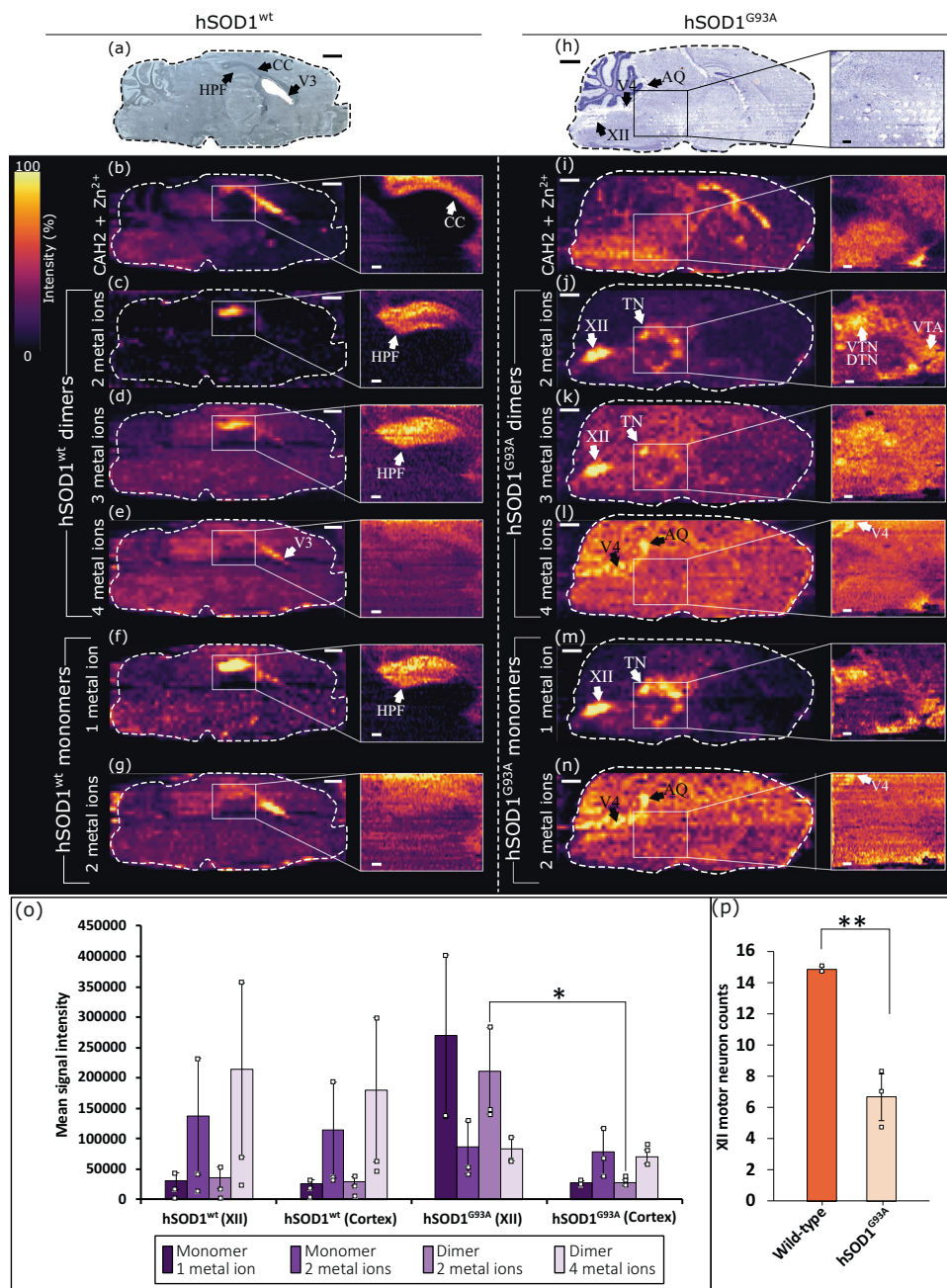


Fig. 3 | Histology and MS images of transgenic mouse brains. **a** optical scan of a section of brain hWT-B2. MS images for **(b)** carbonic anhydrase (CAH) 2 + Zn²⁺, intact hSOD1^{wt} dimers, **(c)** with two metal ions; **d** three metal ions; **e** four metal ions, and monomers with **(f)** one metal ion; **g** two metal ions. Selected regions show high-resolution MSI for the tissue around the hippocampal formation. **h** Nissl-stained (post-MSI) sections of brain G93A-B1. Full section MS images for **(i)** CAH2 + Zn²⁺, intact hSOD1^{G93A} dimers with **(j)** two metal ions; **k** three metal ions; **l** four metal ions, and monomers with **(m)** one metal ion; **n** two metal ions. White boxes show high-resolution MSI. **o** Relative signal intensity of SOD1 complexes in hypoglossal nucleus (XII) and frontal cortex for each genotype (hSOD1^{wt} *N* = 3, hSOD1^{G93A} *N* = 3). Data expressed as mean signal intensity from three sections for each genotype +/-

SD. **p** Average motor neuron counts (+/- SD) in XII from mSOD1^{wt} (*N* = 2, total sections = 12) and hSOD1^{G93A} (*N* = 3, total sections = 15) mice. Students' two-sided *T* test; **P* < 0.05 (actual *P* = 0.027), ***P* < 0.01 (actual *P* = 9.45 × 10⁻³). HPF hippocampal formation, CC corpus callosum, V3 third ventricle, V4 fourth ventricle, AQ cerebral aqueduct, XII hypoglossal nucleus, TN tegmental nuclei, VTN ventral tegmental nucleus, DTN dorsal tegmental nucleus, VTA ventral tegmental area. MS images have one order of linear interpolation applied and a linear intensity scale. Scale bars: Full brain images; 1000 μm, high-resolution MSI; 200 μm, Nissl-stain expanded region; 50 μm. High-resolution MSI was performed on a separate serial section. Source data are provided as a Source Data file.

intramolecular disulfide bond and Cu ions⁴³⁻⁴⁵. The abundance of Zn-bound dimers in the motor-associated regions supports the assertion that maturation is hindered at the disulfide formation/Cu ion incorporation step. An increased oxidative environment in the cytosol of cells in the affected motor regions could cause premature intramolecular disulfide formation prior to interaction with CCS. CCS cannot interact with Zn-bound SOD1 dimers with a preformed disulfide bond,

thus preventing maturation⁴⁴. As described in Supplementary Fig. S10, Supplementary Information, some proportion of the metal-deficient hSOD1^{G93A} dimers (2 metal ions) featured intact disulfide bonds. An insufficient level of Cu for SOD1 maturation has been reported in bulk CNS tissues of the hSOD1^{G37R} mouse model, whereas Zn levels were elevated in line with protein overexpression⁴⁶. Evidence of Cu dyshomeostasis and wild-type SOD1 dysfunction has also been observed in

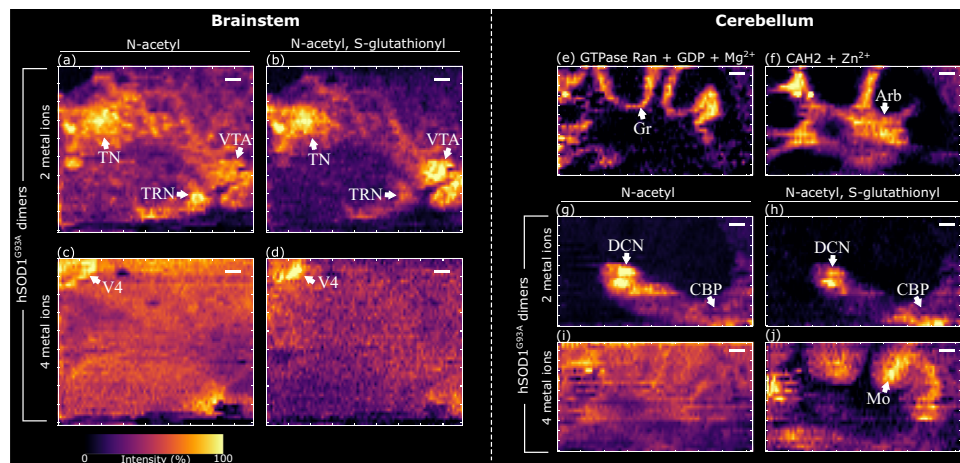


Fig. 4 | High-resolution ion images illustrating protein complex distributions due to PTMs in the brainstem and cerebellum. Brainstem ion images for hSOD1^{G93A} dimers binding two metal ions and comprised of **a** two N-acetyl subunits and **b** one N-acetyl subunit and one N-acetyl, S-glutathionyl subunit; both dimers are distributed in cranial nuclei. hSOD1^{G93A} dimers binding four metal ions and comprised of **c** two N-acetyl subunits and **d** one N-acetyl subunit and one N-acetyl, S-glutathionyl subunit. Cerebellum ion images for **(e)** GTPase Ran + GDP + Mg²⁺ complex in the granular layer and **(f)** CAH2 + Zn²⁺ complex in the arbor vitae (Arb) are shown to assist with orientation of the hSOD1^{G93A} ion images. hSOD1^{G93A} dimers binding two metal ions and comprised of **(g)** two N-acetyl subunits and **(h)** one N-acetyl subunit and one N-acetyl, S-glutathionyl subunit are both localized to grey

matter of the deep cerebellar nuclei (DCN) and cerebellar peduncles (CBP). hSOD1^{G93A} dimers binding four metal ions and comprised of **(i)** two N-acetyl subunits and **(j)** one N-acetyl subunit and one N-acetyl, S-glutathionyl subunit. The former is ubiquitous and the latter abundant in the molecular layer. Ion images are composites of multiple charge states; hSOD1^{G93A} dimers (11⁺, 10⁺, 9⁺), GTPase Ran (9⁺ and 8⁺), CAH2 (9⁺ and 8⁺). Presented with a linear intensity scale, 1 order of linear interpolation, and TIC normalized. TN tegmental nuclei, TRN tegmental reticular nucleus, VTA ventral tegmental area, V4 fourth ventricle, Gr granular layer, Arb arbor vitae, DCN deep cerebellar nuclei, CBP cerebellar peduncles, Mo molecular layer. Scale bars = 200 μm.

regions of neuronal loss in cases of Parkinson's disease which is linked with oxidative stress⁴⁷.

Dimers bound to 3 metal ions exhibit similar localization to the 2 metal-bound dimers, which suggests that the metal deficiency is partially due to inefficient copper incorporation rather than premature disulfide formation exclusively. Low abundance or efficacy of CCS within affected motor regions could result in an increase in the relative abundance of Cu-deficient hSOD1^{G93A} dimers. It is possible that a proportion of the two metal-bound dimers are disulfide-reduced species, as suggested by Tajiri et al.⁴³. In that in vitro study, zinc ions in excess could not be incorporated into the disulfide-reduced dimers beyond one zinc ion per monomer, whereas disulfide-intact dimers were able to bind up to five zinc ions. As the 3 metal-bound dimers exhibit ventral horn and brainstem nuclei localization, it is possible these are dimers with 3 zinc ions.

An alternative explanation could be low availability of Cu ions, eventually leading to the accumulation of Cu-deficient SOD1 species, both soluble and aggregated^{7,48}. Studies in hSOD1^{G93A} and hSOD1^{G37R} mice where the Cu-containing therapeutic Cu(atm) was administered increased SOD1 enzymatic activity by populating Cu-binding sites²⁶, resulting in prolonged survival and protection of motor neurons in the CNS^{26,49,50}. Recent work in sporadic ALS cases in humans also implicates aberrant copper bioavailability in disease progression by broadly affecting cuproenzymes⁵¹. It is also possible that Zn-deficient hSOD1^{G93A} species are present, previously reported to cause motor neuron apoptosis in mice^{52,53} and reported in human spinal cord for various cases of ALS⁵⁴. In summary, the affected regions of CNS tissue inevitably contain a mixed population of Zn and Cu-bound, but overall metal-deficient, hSOD1^{G93A} complexes. Separation of complexes with different metals and disulfide bond states by mass alone is still challenging; further work will require high-resolution MS in tandem with gas phase fractionation methods, e.g., ion mobility spectrometry or ion-ion reactions^{55,56}.

Discussion

Central nervous system tissue sections from transgenic mice expressing human SOD1 were imaged by native ambient MSI. The disease

model, hSOD1^{G93A}, showed abundance of metal-deficient hSOD1^{G93A} complexes in motor-associated structures of the CNS. The distribution indicates a relationship between the cellular environment of the affected motor regions and hSOD1^{G93A} existing in a demetallated state. It may be that the demetallated hSOD1^{G93A} is misfolded and hinders metal ion binding, or demetallation may be a precursor of further misfolding and aggregation. Monomerisation and glutathionylation were not found to influence spatial localization of metal-deficient complexes; metal-binding state remained the key factor. The cause of the loss or omission of metal ions from hSOD1^{G93A} complexes in these tissue structures remains to be explained. We hypothesize that a property of the local cellular environment, e.g., metal ion concentration (insufficient Cu in CNS tissues of the hSOD1^{G37R} model⁴⁶), availability of CCS, pH, etc., is responsible for hSOD1^{G93A} metal ion deficiency.

Current practical limitations prevent elucidation of which metal ions are bound and the status of the disulfide bond in hSOD1^{G93A} complexes during a native ambient MS imaging experiment. MS approaches using ultra-high mass resolving powers are largely incompatible with MSI, although methods have been demonstrated which might be adaptable in the future^{55,56}. Imaging methods using a mode of tandem mass spectrometry approaches or ion mobility spectrometry may be able to reveal further information. Nevertheless, untargeted visualization of protein distributions with specificity for their non-covalent and covalent modifications is a distinctive capability provided by NAMS for neurodegenerative disease pathology.

Overall, these results have implications for understanding the role of SOD1 toxic gain of function in ALS, which is particularly relevant in the context of therapeutics which reduce mutant SOD1 levels in ALS patient CNS, such as Tofersen^{57,58}. The techniques developed here show that demetallation is a key pathological change observed for hSOD1^{G93A} and may help to define whether this mechanism contributes to a broader population of sporadic ALS. Further work will focus on the application of native ambient mass spectrometry imaging of the various hSOD1 species over the time-course of the development of pathology in the model, expansion to additional models and human cases, and continued development of the imaging technology.

Methods

Ethics statement

All studies using animals were carried out in accordance with the UK Animals (Scientific Procedures) Act 1986, and all procedures were carried out under a Home Office project licence, reviewed, and approved by the local ethics committee (University of Sheffield Animal Welfare and Ethical Review Body). All animal maintenance and day-to-day care was carried out in line with Home Office Code of Practice for Housing and Care of Animals Used in Scientific Procedures.

Materials

MS-grade water (catalog number 10095164) was purchased from Fisher Scientific (Loughborough, UK). HPLC-grade ammonium acetate (catalog number 15513351) was bought from J.T. Baker (Deventer, Netherlands). The detergent C_8E_4 (catalog number T3394), SOD1 and IL-2 primers (detailed below), agarose powder (catalog number A9539), and ethidium bromide solution (catalog number E1510) were bought from Sigma-Aldrich (Gillingham, UK). Mass spectrometer calibration was performed with FlexMix (catalog number A39239, Thermo Fisher, San Jose, CA). Nitrogen (>99.995%) and helium (>99.996%) gases used on the mass spectrometer were obtained from BOC (Guildford, UK). QuickExtract DNA extraction solution (catalog number QE09050) was purchased from Cambio Ltd (Cambridge, UK). Master mix (catalog number SBD-04-11-00115) was purchased from Thistle Scientific (Rugby, UK).

Transgenic mice

SOD1^{G93A} C57BL/6 transgenic mice, originally B6SJL-Tg (SOD1^{G93A}) 1Gur/J (stock number 002726) mice were obtained from Jackson Laboratory and backcrossed onto the C57BL/6 OlaHsd background (Harlan UK, C57BL/6J OlaHsd) for at least 20 generations to create the SOD1^{G93A} C57BL/6 transgenic line on an inbred genetic background⁵⁹. The SOD1^{G93A} transgene is maintained as a hemizygous trait by breeding hemizygous males with wild-type female mice (C57BL/6J OlaHsd, Harlan UK). Breeding was performed in-house at the University of Sheffield.

Human SOD1^{wt} mice (B6.Cg-Tg(SOD1)2Gur/J) were obtained from the Jackson Laboratory, strain number 02298²⁰, and these were backcrossed onto the C57BL/6 OlaHsd background (Harlan UK, C57BL/6J OlaHsd) for at least 20 generations. The colony was maintained in-house by breeding female transgenic mice with C57BL/6J mice. This transgenic strain carries the normal allele of human SOD1 and does not carry the SOD1^{G93A} transgene.

Mice were housed in groups of between 2 and 5, with one plastic house provided per cage, sawdust (Datesand) was used to cover the floor of the cage and paper wool bedding (Datesand) was provided as nesting material. All animals were housed in rooms maintained at a temperature of 21 °C and with a 12-h light/dark cycle. Food (standard rodent diet 2018, Evigo) and water were provided ad libitum, with weekly water changes.

Mice were earclipped for the purpose of identification and genotyping. Extraction of DNA from the earclip was performed using 20 µl of Quickextract (Lucigen), with incubation at 65 °C for 15 min followed by 98 °C for 2 min. Genotyping for hSOD1^{G93A} and hSOD1^{wt} mice was carried out using the same protocol. PCRs for genotyping were performed in a 10 µl volume of master mix containing 5x FIREPol Master Mix with 7.5 mM MgCl₂ (Thistle Scientific, UK, SBD-04-11-00115), 150 nmol each of human SOD1 primers (forward 5'-CATCAGCCCTAATCCATCTGA-3', reverse 5'-CGCGACTAACAAATCAAAGTGA-3') and control interleukin-2 receptor (IL-2R) primers (forward 5'-CTAGGCCACAGAATTGAAA GATCT-3', reverse 5'-GTAGGTGGAATTCTAGCATCATC-3'), nuclease-free water, and 0.5 µl of DNA sample. Gel electrophoresis was performed on PCR products on a 2% agarose gel with 1 µl ethidium bromide solution per 100 ml, IL-2R products were visualized at 324 bp and human SOD1, if present in the case of transgenic animals, was present at 236 bp.

Brain and spinal cord tissue

Fresh-frozen tissue. Brains and spinal cords from transgenic mice (120–130 days old, see Supplementary Table S1, Supplementary Information) expressing a mutant human isoform of SOD1, hSOD1^{G93A}, were snap-frozen over dry ice on foil and then stored at –80 °C. Control brains and spinal cords from transgenic mice (120–180 days old, Supplementary Table S1, Supplementary Information) expressing the human wild-type protein (hSOD^{wt}) were prepared in the same way. Lumbar spinal cord tissue was processed as follows; the lumbar enlargement was dissected from the cord and bisected. Lumbar cord coronal sections were collected at 10 µm thickness outwards from the bisection point. Serial sagittal brain sections of 10 µm thickness were prepared from the left-brain hemisphere, cutting outwards from the midline. Cryosections were prepared with a CM1810 Cryostat (Leica Microsystems, Wetzlar, Germany) and thaw mounted to glass microscope slides before storage at –80 °C until analysis. The tissue was not washed or fixed before native ambient mass spectrometry imaging.

Fixed tissue. formalin-fixed paraffin-embedded (FFPE) lumbar spinal cord was prepared from hSOD1^{G93A} transgenic ($N=5$) and mSOD1^{wt} ($N=5$) mice at 120 ± 3 days of age. Lumbar spinal cord (L3/4) was perfused under terminal anesthesia with PBS followed by 4% paraformaldehyde in PBS, then were processed and embedded in wax blocks, sectioned at 10 µm thickness on a microtome and every fifth section arrayed on glass slides. A total of 54 sections were analyzed for motor neurons (hSOD1^{G93A} $N=28$; mSOD1^{wt} $N=36$). FFPE-embedded brainstems were similarly obtained from mice of the same genotypes (hSOD1^{G93A} $N=3$; mSOD1^{wt} $N=2$) for a total of 27 sections (hSOD1^{G93A} $N=15$, mSOD1^{wt} $N=12$).

Native ambient mass spectrometry imaging (MSI)

Native ambient MSI was performed using a home-built nano-DESI ion source attached to an Orbitrap Eclipse mass spectrometer (Thermo Fisher Scientific; Fig. 1) equipped with the high mass range (HMR[®]), electron transfer dissociation (ETD) and proton transfer charge reduction (PTCR) options^{21,24}. The analytical solvent system was aqueous ammonium acetate (200 mM) with 0.125% of the detergent C_8E_4 added by volume. Solvent flow rate was optimized to between 0.5 and 2.0 µl/min, and spray voltage was between 800 and 1300 V. Electrospray stability was assessed using the linear ion trap (LIT) mass analyser by monitoring m/z 307.21 until an RSD% <15% was achieved by tuning flow rate, electrospray voltage and emitter position.

The mass spectrometer was operated in intact protein mode. Typical source backing pressure was 2.3 Torr. The source ion transfer tube temperature was 275–300 °C. The RF lens was set to 120%. Source dissociation voltage (SDV) was set to 80 V, and the source compensation value (SCV) was tuned for each experiment to between 2.5 and 3.2%, as day-to-day differences in ambient temperature and chamber pressures in the mass spectrometer affect the optimal value. The importance of these settings has been discussed elsewhere^{23,60,61}. The ion routing multipole (IRM) was set to a pressure of 20 mTorr using N_{2(g)}. All ion images were collected using a selected ion monitoring (SIM) method (depicted in Fig. 1). Ions were accumulated in the IRM followed by transfer to the LIT. An isolation window of m/z 3197 ± 625 (brain) or m/z 3000 ± 1000 (spinal cord) was applied before transmission of ions to the orbitrap analyzer for mass-to-charge ratio (m/z) measurement. Supplementary collisional activation and an averaging of 5 microscans was used to improve S/N for spinal cord images. The LIT damping gas (He_(g)) pressure was 3.5×10^{-5} Torr. The automatic gain control target was set to 10,000% (5×10^6 charges) with a maximum injection time of 750 ms. The orbitrap analyzer was operated at a resolution setting of 7500 FWHM (at m/z 200, 16 ms transient length). Proceeding with imaging experiments was conditional on achieving a signal intensity >1 × 10⁴ (normalized level) for holo-hSOD1^{G93A} dimer (10+ charge state) under these instrument conditions.

For full brain section (hSOD1^{wt} $N=3$, hSOD1^{G93A} $N=3$) imaging, the tissue was moved under the nano-DESI probe at 20 $\mu\text{m/s}$ with a line step of 200 μm . For spatially targeted high-resolution brain MSI (hSOD1^{wt} $N=1$, hSOD1^{G93A} $N=1$), the movement velocity was 3 $\mu\text{m/s}$ with a line step of 50 μm . Full spinal cord sections (hSOD1^{wt} $N=2$, hSOD1^{G93A} $N=2$) were imaged at 8 $\mu\text{m/s}$ with a line step of 100 μm . High-resolution spinal cord MSI (hSOD1^{G93A} $N=1$) was performed at 3 $\mu\text{m/s}$ with a line step of 30 μm .

Mass spectrometer cycle time was ~1 s with automated analysis of each brain section requiring ~6 h. High-resolution images were analyzed from separate serial sections and required ~11 h to record. Spinal cord analysis required ~3 h per section, and 3 h for high-resolution analysis of the 1 mm \times 0.69 mm region.

Ion image processing

Ion image files were generated by conversion of the Thermo raw files acquired for each line scan to a single imzML file using Firefly (v.3.2.0.23, ProSolia, Inc., Indianapolis, IN). Pixels in full brain section ion images were composed of ten seconds of summed MS scans representing 200 \times 200 μm (0.04 mm²) of tissue and are referred to as “moderate resolution MSI”. Similarly, spinal cord image pixels were composed of scans representing 100 \times 100 μm of tissue (~0.01 mm²). Pixels in spatially targeted, high-resolution MSI had pixel dimensions of 30 \times 50 μm (in brain, representing ~0.0015 mm² of tissue) and 14 \times 30 μm (in spinal cord, ~0.00042 mm²). Ion images were processed in MSiReader (v.1.0.2, North Carolina State University)⁶², had 1 \times linear interpolation applied, and a linear intensity scale normalized to the most intense pixel in the image at the selected $m/z \pm 0.1$. Ion images for each charge state of the hSOD1 dimers, [Arf1+GDP], [Arf3+GDP] and [CAH2 + Zn²⁺] complexes, and β -synuclein were summed using a MATLAB script (available from https://github.com/coopergroup-massspec/sum_matlab_figures, and since facilitated by a high throughput imaging module in UniDec version 6.0.4⁶³) to create images composed of all detected signal for each complex. (Ion images for monomeric SOD1 comprise a single charge state (6+)). Constituent ion images for images comprising multiple protein charge states are found in the Supplementary Information and referenced specifically in the main text. Non-SOD1 protein images were inspected to validate analytical performance between experiments (Supplementary Fig. S30, Supplementary Information).

Top-down MS analysis

For native top-down MS of protein–metal complexes, tissue was sampled by nano-DESI using aqueous ammonium acetate (200 mM) with 0.125% of the detergent C₈E₄ added by volume. Protein–metal complex ions were subject to gas phase dissociation using beam-type collisional activation (HCD) in N_{2(g)} or resonant collision-induced dissociation (CID) in He_(g). The IRM pressure was 20 mTorr and the orbitrap resolution was 240,000 (FWHM at m/z 200, 512 ms transient). Normalized collision energy (NCE) was typically set to 30–35% for dissociation of non-covalent SOD1 complexes and 39–45% for top-down protein sequencing (10+ charge state). Top-down analysis using electron transfer dissociation with supplemental collision activation (ETHCD) was performed with reaction time 10–18 ms, and supplemental collision energy of 10–12%.

Top-down analysis of denatured proteins was performed using contact LESA of tissue with a Triversa Nanomate robot (Advion Biosciences, Ithaca, NY)⁶⁴. The solvent system was acetonitrile/water +0.1% formic acid (1:1 v/v) to dissociate metal ions and unfold hSOD1 in solution. Protein ions were m/z selected using the quadrupole mass filter then fragmented by collisional activation (HCD; NCE 38%) in the IRM (pressure = 8 mTorr). Orbitrap resolution was 240,000 (FWHM at m/z 200).

Fragment ion spectra were automatically matched to theoretical fragment ions with a tolerance of 20 ppm for the hSOD1^{G93A} sequence using ProSight PC (version 4.1, Thermo), followed by manual interpretation and validation.

Spectral deconvolution

Mass spectra were deconvoluted with UniDec (version 6.0.4)⁶⁵ to determine protein complex mass from multiple protein ion charge states from non-isotopically resolved mass spectra. Parameters other than those described in Supplementary Table S7, Supplementary Information were left at default values.

Histology

Nissl staining procedure. Tissue sections were allowed to warm to room temperature before staining. Slides were placed into 95% alcohol for 5 min, followed by 70% alcohol for a further 5 min, and finally washed in tap water. 0.1% Cresyl fast violet solution was first filtered, and slides were then stained for 20 min. Stained sections were differentiated in acetic acid for around 4 s and then washed in 95% alcohol. This differentiation time allowed for sufficient separation between the background and Nissl-stained cells of interest. At this point the sections could be viewed under a microscope to verify the background separation, and the slides could be returned to acetic acid for further differentiation if necessary. Finally, slides were dehydrated in absolute alcohol for 2 \times 5 min before being cleared in xylene and coverslips mounted with DPX.

Optical scanning and tissue annotation

Stained tissue sections were scanned at $\times 20$ –40 magnification using a Hamamatsu Nanoscope XR. Scanned sections were visualized with QuPath version 0.4.1⁶⁶. Tissue was annotated with reference to the Allen Adult Mouse Atlas⁶⁷.

Statistical analysis

Evaluation of relative abundances of SOD1 complexes (Figs. 2o and 3o). The mean signal intensity of each complex (in dorsal horns; $n=4$, ventral horns; $n=4$, XII; $n=3$, frontal cortex; $n=3$) for each genotype was averaged. Charge states 11+, 10+ and 9+ were included for SOD1 dimers; for monomers, 6+ and 5+. The 10+ dimers and 5+ monomers overlap in m/z in the imaging datasets, but high-resolution mass spectrometry was used to estimate a 52% contribution to signal intensity by the 10+ dimers (Supplementary Fig. S31, Supplementary Information). The statistical significance of signal intensity differences between VH and DH, and XII and frontal cortex, were evaluated by Student’s unpaired T test.

Motor neuron counts in the ventral horn (Fig. 2p). Nissl-stained and lumbar ventral horn motor neurons were counted from intact hemisections from each genotype (hSOD1^{G93A} sections = 28, mSOD^{wt} sections = 36). Motor neurons were distinguished based on location (ventral horn) and morphological criteria as follows: large multipolar cells, cell body with a size of at least 25 μm in any one dimension, a distinct nucleus and nucleolus. An average number of motor neurons were then determined for each mouse ($N=5$ hSOD1^{G93A} transgenic mice and $N=5$ non-transgenic mice) genotype and analyzed by unpaired T test.

Motor neuron counts in the hypoglossal nucleus (XII, (Fig. 3p). Motor neurons were counted, as for the spinal cord, in FFPE brainstem sections (hSOD1^{G93A} sections = 15, mSOD^{wt} sections = 12) for each mouse genotype (hSOD1^{G93A} $N=3$, mSOD^{wt} $N=2$).

Reporting summary

Further information on research design is available in the Nature Portfolio Reporting Summary linked to this article.

Data availability

The mass spectrometry and optical imaging data generated in this study have been deposited in the University of Birmingham

Institutional Research Archive under accession code [<https://doi.org/10.25500/edata.bham.00001123>]. Processed data are also available in the same archive. Mass spectrometry data have also been deposited to the ProteomeXchange Consortium via the PRIDE partner repository with the dataset identifier PXD053247 [<https://www.ebi.ac.uk/pride/archive/projects/PXD053247>]. The signal intensity and motor neuron count data generated in this study are provided in the Source Data file. Source data are provided with this paper.

Code availability

Code for the generation of composite ion images²³ is available from https://github.com/coopergroup-massspec/sum_matlab_figures and <https://doi.org/10.5281/zenodo.12572632>.

References

- Robberecht, W. & Philips, T. The changing scene of amyotrophic lateral sclerosis. *Nat. Rev. Neurosci.* **14**, 248–264 (2013).
- Julien, J. P. Amyotrophic lateral sclerosis: unfolding the toxicity of the misfolded. *Cell* **104**, 581–591 (2001).
- Hilton, J. B., White, A. R. & Crouch, P. J. Metal-deficient SOD1 in amyotrophic lateral sclerosis. *J. Mol. Med. (Berl.)* **93**, 481–487 (2015).
- Tokuda, E. et al. A copper-deficient form of mutant Cu/Zn-superoxide dismutase as an early pathological species in amyotrophic lateral sclerosis. *Biochim Biophys. Acta Mol. Basis Dis.* **1864**, 2119–2130 (2018).
- Tiwari, A. et al. Metal deficiency increases aberrant hydrophobicity of mutant superoxide dismutases that cause amyotrophic lateral sclerosis. *J. Biol. Chem.* **284**, 27746–27758 (2009).
- Svensson, A. K. et al. Metal-free ALS variants of dimeric human Cu,Zn-superoxide dismutase have enhanced populations of monomeric species. *PLoS ONE* **5**, e10064 (2010).
- Bourassa, M. W., Brown, H. H., Borchelt, D. R., Vogt, S. & Miller, L. M. Metal-deficient aggregates and diminished copper found in cells expressing SOD1 mutations that cause ALS. *Front. Aging Neurosci.* **6**, 110 (2014).
- Karch, C. M., Prudencio, M., Winkler, D. D., Hart, P. J. & Borchelt, D. R. Role of mutant SOD1 disulfide oxidation and aggregation in the pathogenesis of familial ALS. *Proc. Natl. Acad. Sci. USA* **106**, 7774–7779 (2009).
- Anzai, I. et al. A misfolded dimer of Cu/Zn-superoxide dismutase leading to pathological oligomerization in amyotrophic lateral sclerosis. *Protein Sci.* **26**, 484–496 (2017).
- Rakhit, R. et al. Monomeric Cu,Zn-superoxide dismutase is a common misfolding intermediate in the oxidation models of sporadic and familial amyotrophic lateral sclerosis. *J. Biol. Chem.* **279**, 15499–15504 (2004).
- Brujin, L. I. et al. Aggregation and motor neuron toxicity of an ALS-linked SOD1 mutant independent from wild-type SOD1. *Science* **281**, 1851–1854 (1998).
- Redler, R. L. et al. Glutathionylation at Cys-111 induces dissociation of wild type and FALS mutant SOD1 dimers. *Biochemistry* **50**, 7057–7066 (2011).
- McAlary, L., Yerbury, J. J. & Aquilina, J. A. Glutathionylation potentiates benign superoxide dismutase 1 variants to the toxic forms associated with amyotrophic lateral sclerosis. *Sci. Rep.* **3**, 3275 (2013).
- Pare, B. et al. Misfolded SOD1 pathology in sporadic amyotrophic lateral sclerosis. *Sci. Rep.* **8**, 14223 (2018).
- Bosco, D. A. et al. Wild-type and mutant SOD1 share an aberrant conformation and a common pathogenic pathway in ALS. *Nat. Neurosci.* **13**, 1396–1403 (2010).
- Grad, L. I. et al. Intercellular propagated misfolding of wild-type Cu/Zn superoxide dismutase occurs via exosome-dependent and -independent mechanisms. *Proc. Natl. Acad. Sci. USA* **111**, 3620–3625 (2014).
- Forsberg, K. et al. Misfolded SOD1 inclusions in patients with mutations in C9orf72 and other ALS/FTD-associated genes. *J. Neurol. Neurosurg. Psychiatry* **90**, 861–869 (2019).
- Kerman, A. et al. Amyotrophic lateral sclerosis is a non-amyloid disease in which extensive misfolding of SOD1 is unique to the familial form. *Acta Neuropathol.* **119**, 335–344 (2010).
- Ayers, J. I. et al. Conformational specificity of the C4F6 SOD1 antibody; low frequency of reactivity in sporadic ALS cases. *Acta Neuropathol. Commun.* **2**, 55 (2014).
- Gurney, M. E. et al. Motor neuron degeneration in mice that express a human Cu,Zn superoxide dismutase mutation. *Science* **264**, 1772–1775 (1994).
- Hale, O. J. & Cooper, H. J. Native mass spectrometry imaging of proteins and protein complexes by nano-DESI. *Anal. Chem.* **93**, 4619–4627 (2021).
- Hale, O. J. & Cooper, H. J. Native ambient mass spectrometry of an intact membrane protein assembly and soluble protein assemblies directly from lens tissue. *Angew. Chem. Int. Ed. Engl.* **61**, e202201458 (2022).
- Hale, O. J., Hughes, J. W., Sisley, E. K. & Cooper, H. J. Native ambient mass spectrometry enables analysis of intact endogenous protein assemblies up to 145 kDa directly from tissue. *Anal. Chem.* **94**, 5608–5614 (2022).
- Sisley, E. K., Hale, O. J., Styles, I. B. & Cooper, H. J. Native ambient mass spectrometry imaging of ligand-bound and metal-bound proteins in rat brain. *J. Am. Chem. Soc.* **144**, 2120–2128 (2022).
- Sussulini, A., Becker, J. S. & Becker, J. S. Laser ablation ICP-MS: application in biomedical research. *Mass Spectrom. Rev.* **36**, 47–57 (2017).
- Roberts, B. R. et al. Oral treatment with Cu(II)(atSm) increases mutant SOD1 in vivo but protects motor neurons and improves the phenotype of a transgenic mouse model of amyotrophic lateral sclerosis. *J. Neurosci.* **34**, 8021–8031 (2014).
- Acquadro, E. et al. Human SOD1-G93A specific distribution evidenced in murine brain of a transgenic model for amyotrophic lateral sclerosis by MALDI imaging mass spectrometry. *J. Proteome Res.* **13**, 1800–1809 (2014).
- Roach, P. J., Laskin, J. & Laskin, A. Nanospray desorption electrospray ionization: an ambient method for liquid-extraction surface sampling in mass spectrometry. *Analyst* **135**, 2233–2236 (2010).
- Kertesz, V. & Van Berkel, G. J. Fully automated liquid extraction-based surface sampling and ionization using a chip-based robotic nanoelectrospray platform. *J. Mass Spectrom.* **45**, 252–260 (2010).
- Sarsby, J., Martin, N. J., Lalor, P. F., Bunch, J. & Cooper, H. J. Top-down and bottom-up identification of proteins by liquid extraction surface analysis mass spectrometry of healthy and diseased human liver tissue. *J. Am. Soc. Mass Spectrom.* **25**, 1953–1961 (2014).
- Kim, R. B., Irvin, C. W., Tilva, K. R. & Mitchell, C. S. State of the field: an informatics-based systematic review of the SOD1-G93A amyotrophic lateral sclerosis transgenic mouse model. *Amyotroph. Lateral Scler. Frontotemporal Degener.* **17**, 1–14 (2015).
- Fanelli, F. et al. Age-dependent roles of peroxisomes in the hippocampus of a transgenic mouse model of Alzheimer's disease. *Mol. Neurodegener.* **8**, 8 (2013).
- Winer, L. et al. SOD1 in cerebral spinal fluid as a pharmacodynamic marker for antisense oligonucleotide therapy. *JAMA Neurol.* **70**, 201–207 (2013).
- Smith, R., Myers, K., Ravits, J. & Bowser, R. Amyotrophic lateral sclerosis: is the spinal fluid pathway involved in seeding and spread? *Med Hypotheses* **85**, 576–583 (2015).
- Lin, Z. F. et al. SIRT5 desuccinylates and activates SOD1 to eliminate ROS. *Biochem. Biophys. Res. Commun.* **441**, 191–195 (2013).
- Prell, T. & Grosskreutz, J. The involvement of the cerebellum in amyotrophic lateral sclerosis. *Amyotroph. Lateral Scler. Frontotemporal Degener.* **14**, 507–515 (2013).

37. Pradat, P. F. The cerebellum in ALS: friend or foe? *J. Neurol. Neurosurg. Psychiatry* **92**, 1137 (2021).
38. Bede, P. et al. Genotype-associated cerebellar profiles in ALS: focal cerebellar pathology and cerebro-cerebellar connectivity alterations. *J. Neurol. Neurosurg. Psychiatry* **92**, 1197–1205 (2021).
39. Kuper, M., Thurling, M., Maderwald, S., Ladd, M. E. & Timmann, D. Structural and functional magnetic resonance imaging of the human cerebellar nuclei. *Cerebellum* **11**, 314–324 (2012).
40. Williams, J. R. et al. Copper delivery to the CNS by CuATSM effectively treats motor neuron disease in SOD(G93A) mice co-expressing the copper-chaperone-for-SOD. *Neurobiol. Dis.* **89**, 1–9 (2016).
41. Hottinger, A. F., Fine, E. G., Gurney, M. E., Zurn, A. D. & Aebischer, P. The copper chelator d-penicillamine delays onset of disease and extends survival in a transgenic mouse model of familial amyotrophic lateral sclerosis. *Eur. J. Neurosci.* **9**, 1548–1551 (1997).
42. Tokuda, E. et al. Ammonium tetrathiomolybdate delays onset, prolongs survival, and slows progression of disease in a mouse model for amyotrophic lateral sclerosis. *Exp. Neurol.* **213**, 122–128 (2008).
43. Tajiri, M. et al. Metal distribution in Cu/Zn-superoxide dismutase revealed by native mass spectrometry. *Free Radic. Biol. Med.* **183**, 60–68 (2022).
44. Furukawa, Y., Torres, A. S. & O'Halloran, T. V. Oxygen-induced maturation of SOD1: a key role for disulfide formation by the copper chaperone CCS. *EMBO J.* **23**, 2872–2881 (2004).
45. Culotta, V. C. et al. The copper chaperone for superoxide dismutase. *J. Biol. Chem.* **272**, 23469–23472 (1997).
46. Hilton, J. B., White, A. R. & Crouch, P. J. Endogenous Cu in the central nervous system fails to satiate the elevated requirement for Cu in a mutant SOD1 mouse model of ALS. *Metallomics* **8**, 1002–1011 (2016).
47. Trist, B. G. et al. Amyotrophic lateral sclerosis-like superoxide dismutase 1 proteinopathy is associated with neuronal loss in Parkinson's disease brain. *Acta Neuropathol.* **134**, 113–127 (2017).
48. Brotherton, T. E., Li, Y. & Glass, J. D. Cellular toxicity of mutant SOD1 protein is linked to an easily soluble, non-aggregated form in vitro. *Neurobiol. Dis.* **49**, 49–56 (2013).
49. Hilton, J. B., Kysenius, K., White, A. R. & Crouch, P. J. The accumulation of enzymatically inactive cuproenzymes is a CNS-specific phenomenon of the SOD1(G37R) mouse model of ALS and can be restored by overexpressing the human copper transporter hCTR1. *Exp. Neurol.* **307**, 118–128 (2018).
50. Soon, C. P. W. et al. Diacetylbis(N(4)-methylthiosemicarbazonato) copper(II) (Cull(atasm)) protects against peroxynitrite-induced nitrosative damage and prolongs survival in amyotrophic lateral sclerosis mouse model. *J. Biol. Chem.* **286**, 44035–44044 (2011).
51. Hilton, J. B. W. et al. Evidence for disrupted copper availability in human spinal cord supports Cu(II)(atasm) as a treatment option for sporadic cases of ALS. *Sci. Rep.* **14**, 5929 (2024).
52. Garner, M. A. et al. Cu,Zn-superoxide dismutase increases toxicity of mutant and zinc-deficient superoxide dismutase by enhancing protein stability. *J. Biol. Chem.* **285**, 33885–33897 (2010).
53. Estevez, A. G. et al. Induction of nitric oxide-dependent apoptosis in motor neurons by zinc-deficient superoxide dismutase. *Science* **286**, 2498–2500 (1999).
54. Trist, B. G. et al. Altered SOD1 maturation and post-translational modification in amyotrophic lateral sclerosis spinal cord. *Brain* **145**, 3108–3130 (2022).
55. Rhoads, T. W. et al. Using theoretical protein isotopic distributions to parse small-mass-difference post-translational modifications via mass spectrometry. *J. Am. Soc. Mass Spectrom.* **24**, 115–124 (2013).
56. Franklin, R., Hare, M. & Beckman, J. S. In *Proteiform Identification: Methods and Protocols* (eds Sun, L. & Liu, X.) 201–210 (Springer US, 2022).
57. Miller, T. et al. Phase 1-2 trial of antisense oligonucleotide tofersen for SOD1 ALS. *New Engl. J. Med.* **383**, 109–119 (2020).
58. Miller, T. M. et al. Trial of antisense oligonucleotide tofersen for SOD1 ALS. *New Engl. J. Med.* **387**, 1099–1110 (2022).
59. Mead, R. J. et al. Optimised and rapid pre-clinical screening in the SOD1(G93A) transgenic mouse model of amyotrophic lateral sclerosis (ALS). *PLoS ONE* **6**, e23244 (2011).
60. Gault, J. et al. Combining native and 'omics' mass spectrometry to identify endogenous ligands bound to membrane proteins. *Nat. Methods* **17**, 505–508 (2020).
61. McGee, J. P. et al. Voltage rollercoaster filtering of low-mass contaminants during native protein analysis. *J. Am. Soc. Mass Spectrom.* **31**, 763–767 (2020).
62. Robichaud, G., Garrard, K. P., Barry, J. A. & Muddiman, D. C. MSiReader: an open-source interface to view and analyze high resolving power MS imaging files on Matlab platform. *J. Am. Soc. Mass Spectrom.* **24**, 718–721 (2013).
63. Hale, O. J., Cooper, H. J. & Marty, M. T. High-throughput deconvolution of native protein mass spectrometry imaging data sets for mass domain analysis. *Anal. Chem.* **95**, 14009–14015 (2023).
64. Randall, E. C., Bunch, J. & Cooper, H. J. Direct analysis of intact proteins from *Escherichia coli* colonies by liquid extraction surface analysis mass spectrometry. *Anal. Chem.* **86**, 10504–10510 (2014).
65. Marty, M. T. et al. Bayesian deconvolution of mass and ion mobility spectra: from binary interactions to polydisperse ensembles. *Anal. Chem.* **87**, 4370–4376 (2015).
66. Bankhead, P. et al. QuPath: open source software for digital pathology image analysis. *Sci. Rep.* **7**, 16878 (2017).
67. Dong, H. W. *The Allen Reference Atlas: A Digital Color Brain Atlas of the C57Bl/6J Male Mouse* (John Wiley & Sons Inc, 2008).

Acknowledgements

O.J.H. and H.J.C. acknowledge EPSRC (EP/S002979/1) for funding. The Orbitrap Eclipse mass spectrometer used in this work was funded by BBSRC (BB/S019456/1).

Author contributions

O.J.H.: study design, tissue preparation, mass spectrometry, data processing, manuscript draft, and review. T.R.W.: tissue collection and histology and manuscript review. R.J.M.: study design, tissue collection, manuscript review. H.J.C.: study design, data analysis, manuscript draft, and review.

Competing interests

The authors declare no competing interests.

Additional information

Supplementary information The online version contains supplementary material available at <https://doi.org/10.1038/s41467-024-50514-7>.

Correspondence and requests for materials should be addressed to Richard J. Mead or Helen J. Cooper.

Peer review information *Nature Communications* thanks Joseph S Beckman, and the other, anonymous, reviewer(s) for their contribution to the peer review of this work. A peer review file is available.

Reprints and permissions information is available at <http://www.nature.com/reprints>

Publisher's note Springer Nature remains neutral with regard to jurisdictional claims in published maps and institutional affiliations.

Open Access This article is licensed under a Creative Commons Attribution 4.0 International License, which permits use, sharing, adaptation, distribution and reproduction in any medium or format, as long as you give appropriate credit to the original author(s) and the source, provide a link to the Creative Commons licence, and indicate if changes were made. The images or other third party material in this article are included in the article's Creative Commons licence, unless indicated otherwise in a credit line to the material. If material is not included in the article's Creative Commons licence and your intended use is not permitted by statutory regulation or exceeds the permitted use, you will need to obtain permission directly from the copyright holder. To view a copy of this licence, visit <http://creativecommons.org/licenses/by/4.0/>.

© The Author(s) 2024